Journal of The
Electrochemical Society

Proton Exchange Membrane Water Electrolyzer Cathode: A Nanomechanical and Nanoelectrical Analysis

Journal of The Electrochemical Society, 2025 **172** 054511

Proton Exchange Membrane Water Electrolyzer Cathode: A Nanomechanical and Nanoelectrical Analysis

Julian Borowec,[1,2,z] Jean-Pierre Poc,[1,2] Shibabrata Basak,[1] Ladislaus Dobrenizki,[3] Günter Schmid,[3] Eva Jodat,[1] André Karl,[1] Rüdiger-A. Eichel,[1,2,4] and Florian Hausen[1,2,z]

[1]*Institute of Energy Technologies - Fundamental Electrochemistry (IET-1), Forschungszentrum Jülich GmbH, 52425 Jülich, Germany*
[2]*Institute of Physical Chemistry, RWTH Aachen University, 52074 Aachen, Germany*
[3]*SE TI SES PRM (Sustainable Energy Solutions - Product - Management), Siemens Energy Global GmbH & Co. KG, 91058 Erlangen, Germany*
[4]*Faculty of Mechanical Engineering, RWTH Aachen University, 52062 Aachen, Germany*

Investigating the aging of proton exchange membrane electrolyzer cells (PEMECs) is crucial for extending their lifetime. Thus, nanomechanical and nanoelectrical atomic force microscopy (AFM) techniques and nanoindentation were employed on a more than 5000 h operated web-woven reinforced membrane electrode assembly (MEA) cathode. Upon operation, a heterogenization and a slight increase in the mean reduced modulus and hardness was observed by nanoindentation. AFM revealed the surface distribution of low stiffness and electrically non-conductive ionomer and high stiffness electrically conductive catalyst particles on the pristine and operated cathodes. The μm sized ionomer plateaus on the surface exhibit a stable nature, as their stiffness and their frequency on the surface remained constant. The operated cathode's catalyst equally stiffened at the two analyzed domains—at positions within carbon fiber (CF) porous transport layer (PTL) imprints and outside of imprints. Thus, no enhanced aging due to local compression is indicated. This study enhances the understanding of cathode aging with respect to the PTL.
 [DOI: 10.1149/1945-7111/add213]

Manuscript submitted December 31, 2024; revised manuscript received April 3, 2025. Published May 19, 2025. *This paper is part of the JES Focus Issue on Proton Exchange Membrane Fuel Cell and Proton Exchange Membrane Water Electrolyzer Durability III.*

Supplementary material for this article is available online

A key to the commercialization of green hydrogen production with proton exchange membrane electrolyzer cells (PEMECs) is the optimization of their core component, the membrane electrode assembly (MEA). The harsh acidic environment in PEMECs necessitates the use of costly precious metal catalysts and causes aging to the MEA and other components.[1–8] Ionomers are a crucial MEA material, which are utilized for the membrane and as part of the catalyst layer. Ionomer membranes undergo performance decay and durability restriction due to poisoning,[9] thermal,[10] mechanical,[11] or chemical degradation.[12–14] The relationship of mechanical and chemical stressors is not yet fully understood.[15] In proton exchange membrane fuel cells (PEMFCs), mechanical compression of the ionomer membrane was reported to change the ionomer's nanostructure and results in an increased chemical degradation,[16] while a recent report found an insignificant effect of tensile stress on the chemical degradation.[17] In a PEMEC, chemical degradation was reported to result in a loss of mechanical integrity.[18] The nanomechanics are also influenced by the ionomer's treatment history,[19] which also determines its nanostructure and ion conducting properties.[20,21]

In catalyst layers, ionomer is present in the form of larger agglomerates and thinner ionomer films surrounding the electrically conductive catalyst particles.[22] Studying an operated cathode side, a slight decrease of fluorine, indicating the ionomer, compared to Pt was observed by energy-dispersive X-ray spectroscopy (EDX).[23] A loss of ionomer in PEMWE is associated with hydrogen peroxide attack on the perfluorosulfonic acid (PFSA) backbone.[24] In another study, the conductive area of the cathode surface was found to remain the same,[25] which indicates a constant ionomer surface coverage with operation. Recently, the crucial role of the catalyst layer and PTL interface at the anode were revealed.[5,26,27] At PTL contacts, a study reports a morphological impact of the fibrous PTL and an apparently thinned electrode at these compressed regions. The authors suggest, based on plasma focused ion beam with scanning electron microscopy (pFIB-SEM) images, that the PTL-fiber-compressed region contained smaller pores.[28] Moreover, a locally increased current density at PTL contacts, especially at the interface of PTL land and channel interface was reported.[29]

The investigations in this work are part of the flagship project DERIEL of the german H2Giga initiative that covers a wide spectrum ranging from small individual laboratory cells to application-oriented test stations in the kW and MW range.[30] Under this framework, the anode of the long-term operated (>5000 h) web-woven fiber reinforced PEMEC MEA was previously nanomechanically and nanoelectrically investigated and a local influence of the expanded metal grid PTL on the anode aging was reported.[26,27] The results on the anode and cross sections are herein extended by analysis of the respective cathode. The advanced high resolution methods nanoindentation,[31] and the current-sensing and force-distance curve based PeakForce Tunneling Atomic Force Microscopy (PF-TUNA) are utilized.[32] The aim is to resolve the local cathode's catalyst and ionomer distribution and aging effects with respect to local carbon fiber (CF) PTL compressed features by nanoelectrical and nanomechanical means. A homogeneous and stable ionomer and catalyst distribution during operation, independent of CF PTL contact points, is essential for preventing localized hot-spot or passivated region formation. Thus, this study provides deeper insights into the microstructural cathode aging, which is critical for designing electrodes with optimized and durable electric, ionic, and mass transport properties.

Results and Discussion

Microscopy analysis.—Figure 1a shows a scanning electron microscopy (SEM) image of a pristine cathode. An operated cathode, displayed in Fig. 1b, exhibits long and several μm thick fibrous marks. The randomly oriented fibrous marks are associated with imprints of the CF PTL, which was in cathode contact during electrolysis.

[z]E-mail: j.borowec@fz-juelich.de; f.hausen@fz-juelich.de

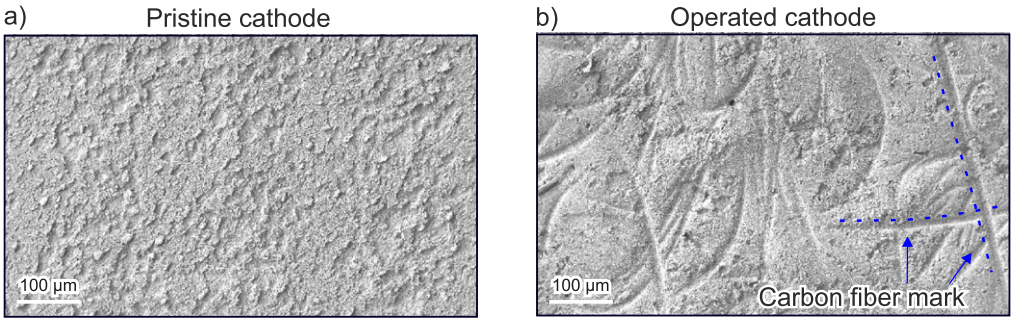

Figure 1. (a) The SEM image exhibits a pristine cathode. (b) An image of an operated cathode displays randomly oriented long and several μm thick fiber marks. These marks are associated with former contact points with the CF PTL. Examplary CF marks are indicated by the dashed blue lines.

Nanomechanics.—The nanomechanical properties of the pristine and operated cathodes are assesed by the analysis of nanoindentation maps. The maps were acquired on four pristine positions (P1-P4) and four operated positions (O1-O4) centrally located between the MEA's water inlet and outlet. More details about the analyzed positions are displayed in Fig. S1. By analyzing the nanoindentation maps, of which examples are given in Fig. S2, a heterogenization of the cathode with operation was found with an additional slight increase of the average reduced modulus and hardness. In the following, more insights into the evaluation are given.

Figure 2a displays the mean reduced modulus of pristine (P1-P4) and operated (O1-O4) cathode positions. The reduced modulus value obtained for each position was averaged from the analysis of an $18 \cdot 18$ indent map covering an area of $360\ \mu m \cdot 360\ \mu m$. The pristine positions exhibit mean reduced moduli ranging from 329.1 MPa to 746.5 MPa. Position P-2 exhibits a significantly lower reduced modulus than the other positions. The statistical deviations indicate slight nanomechanical variations within the analyzed $360\ \mu m \cdot 360 \mu m$ areas. Based on optical microscope images, such as displayed in Fig. S2, the local variations appear random. After long-term operation, the mean reduced modulus values of positions O-1 to O-4 range from 254.2 MPa to 1100.6 MPa with larger statistical deviations within each $360\ \mu m \cdot 360\ \mu m$ area. Averaging the results of all indents that were acquired on pristine and operated positions respectively, reveals a slight increase of the overall mean reduced modulus and a heterogenization of the cathode is observed with operation.

Figure 2b shows the hardness results, which were calculated from the same indents as for the reduced modulus calculations. The analysis of pristine samples exhibits similar mean hardness values, ranging from 67.2 MPa to 87.3 MPa with statistical deviations within the $360\ \mu m \cdot 360\ \mu m$ areas spanning from 19.5 MPa to 28.8 MPa. After operation, mean hardnesses ranging from 71.9 MPa to 144.8 MPa with statistical deviations within the $360\ \mu m \cdot 360\ \mu m$ areas ranging from 45.8 MPa to 64.5 MPa are observed. Averaging all indents that were acquired on pristine and operated positions respectively, a slight increase of the overall mean hardness and a heterogenization of the cathode with operation is observed, which is in agreement with the reduced modulus data. Thus, a comparable trend as for the reduced modulus is observed. Interestingly, the reduced modulus outliers P-2 and O-3 are not noticeable in the hardness analysis. In general, the nanoindentation results are resembling nanoindentation results from MEA catalysts layers reported in literature.[33–35]

The individual components of the cathode catalyst layer, namely Pt catalyst particles, ionomer and pores, influence the nanomechanical properties. In addition to the catalyst layer, the underlying membrane and the interface to the catalyst layer might play a role in the nanomechanical response. Subsequently, the heterogenization and slightly increased reduced modulus and hardness of the cathode with operation indicates a change in one or more of these factors. First, the ionomer might have been physically or chemically altered.

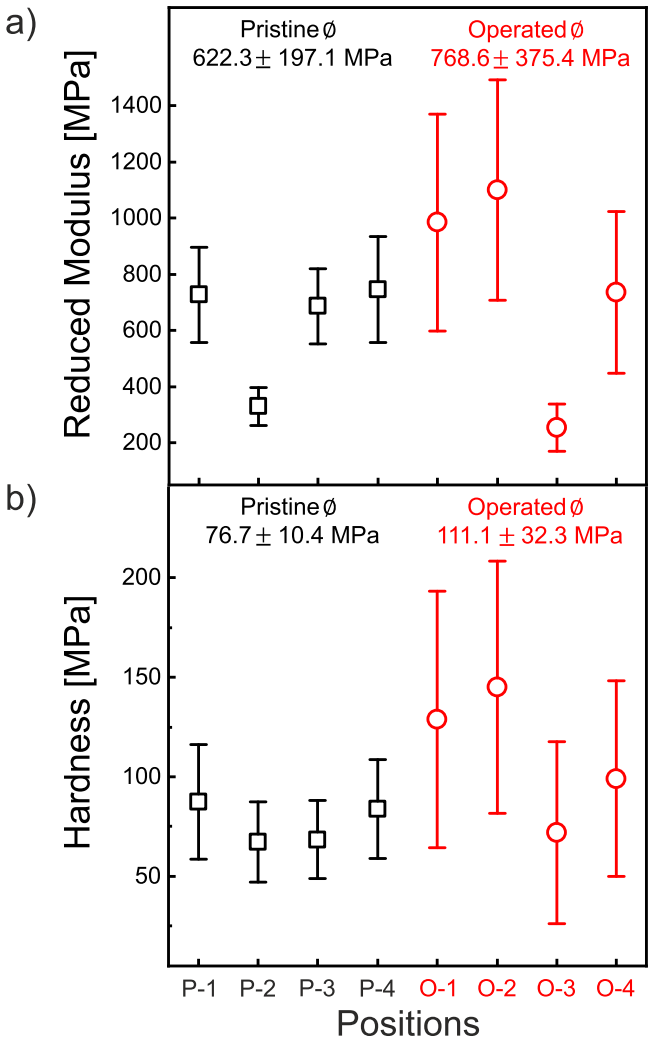

Figure 2. (a) The reduced moduli of the pristine cathode positions P-1, P-3, and P-4 cathode positions indicate comparable nanomechanical properties with an outlier at position P-2. Analysis of operated positions (O1-O4) shows a heterogenization upon operation with a slightly increased overall mean reduced modulus. Comparable to the pristine cathode, one outlier position (O-3) exhibits lower reduced moduli values. (b) The corresponding hardness results exhibit an overall increased mean hardness of the cathode with operation. Moreover, a heterogenization of the operated sample is observed. Each position's mean value was averaged from $18 \cdot 18$ indent maps spanning over $360\ \mu m \cdot 360\ \mu m$ areas (see Figs. S1-S2). Averaging all individual indents of the pristine and operated position respectively, yields the overall averaged values given in the top of each diagram.

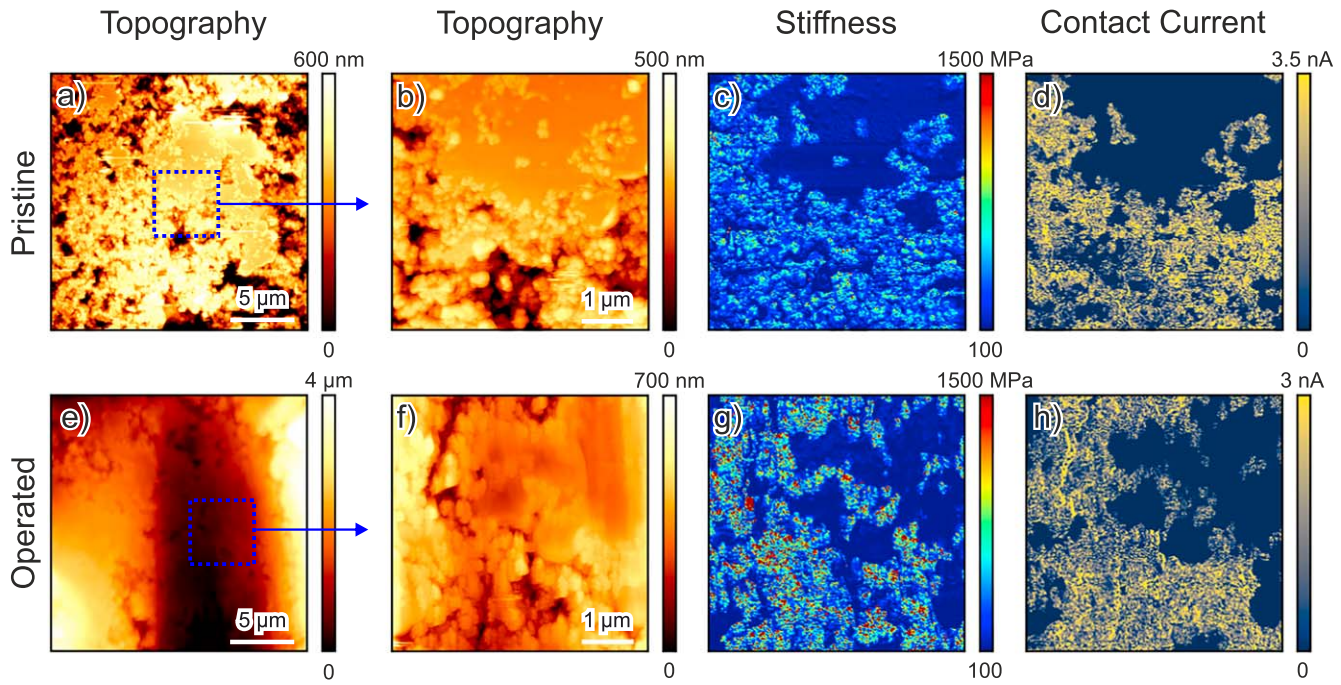

Figure 3. (a) The AFM scan exhibits a pristine cathode topography with a blue dotted box indicating the area of subsequently shown magnifications. (b) The 5 µm · 5 µm topography shows a plateau-like structure in the upper part and rougher particle like structures in the lower part. (c) The corresponding stiffness map shows the lower stiffness of the plateau-like area and higher stiffness of the rough particle-like structures. (d) The respective contact current map shows the electrically insulating nature of the plateau-like low stiffness area, thus, this area is associated with the ionomer. The particle-like stiff area is electrically conductive and thus, associated with the Pt catalyst particles. (e) A larger AFM scan of the operated cathode exhibits a topography map with a CF PTL imprint. The dotted blue box displays the magnified area shown in the next maps. (f)–(h) The 5 µm · 5 µm topography, stiffness, and contact current maps within the CF PTL imprint show comparable features as in (b)-(d).

Second, a decrease of porosity, e.g. by compression during operation, might have increased the effective load-bearing cross sectional area. A decrease in porosity with operation was reported in literature.[28] Local deviations in compression might contribute to the statistical hardness and reduced modulus deviations. Third, a compositional change of the operated cathode might lead to a reduced fraction of soft and low stiffness ionomer relative to the hard and high stiffness Pt catalyst fraction. While a decrease of F, representing the ionomer, compared to Pt with operation was reported in literature,[23] there is also a study, where the ratio remains constant at least on the cathode surface.[25] Ionic contaminants might also compromise the mechanical stability,[36] due to interactions with the PFSA. Fourth, also interfacial changes between membrane and catalyst layer might have altered the load transfer between those.

As the origin of the nanomechanical changes is unclear, surface sensitive PF-TUNA analysis of the cathode was performed to evaluate the surface contribution to the overall nanomechanical cathode change. While the 360 µm · 360 µm nanoindentation maps consist of a few µ*m* deep indents, PF-TUNA results were acquired on 5 µm · 5 µm areas with indents of only a few nm. First, the ionomer and catalyst particle distribution on the catalyst layer surface is discussed. Second, the quantitative analysis of nanomechanical properties is presented, where it was found that the ionomer stiffness remained constant, while the catalyst particles stiffened with operation.

Figure 3a exhibits a 20 µm · 20 µm topography map of a pristine cathode. Rough areas and plateau-like structures are observed. A blue dotted box displays the area, that is subsequently shown in magnified recorded 5 µm · 5 µm maps. The topography map (Fig. 3b) comprises a plateau-like structure in the upper part and rougher particle-like structures in the lower part. The simultaneously acquired corresponding stiffness map (Fig. 3c) and the respective contact current map (Fig. 3d) exhibit that the plateau-like areas are electrically insulating and have a low stiffness. The particle-like stiff areas are mostly electrically conductive. An operated 20 µm · 20 µm cathode scan exhibits a topography map with an around 10 µm thick and long CF PTL imprint. The dotted blue box displays the area shown in the next magnified acquired maps. The 5 µm · 5 µm topography, stiffness, and contact current maps within the CF PTL imprint (Figs. 3f–3h) show comparable features as the pristine maps in Figs. 3b–3d.

The particle-like stiff areas are mostly electrically conductive, and thus, are associated with the Pt catalyst particles. The electrically insulating and low stiffness areas are associated with the ionomer. Both, pristine and operated cathode, exhibit fractions of ionomer and catalyst particles on the surface. On the operated cathode, a significant imprint by the CF PTL is observed. To evaluate the local CF PTL influence on the properties, the in-depth analysis of the shown selective positions needs to be extended by the analysis of multiple positions of pristine and operated cathode samples, followed by a statistical evaluation.

The statistical evaluation was performed by acquiring multiple 5 µm · 5 µm PF-TUNA stiffness maps across the pristine and operated cathode. Ten scans were acquired on a pristine sample and twelve scans on an operated sample—six of them outside of CF PTL imprints and six on areas within CF PTL imprints. The scans were performed on two samples cut from the MEA, as shown in Fig. S1. On each sample the scanned positions were distanced in the mm range from each other. An exemplary histogram evaluation of the stiffness map, shown in Fig. 3c, is depicted in Fig. 4a. The histogram exhibits the number of pixels with the respective stiffness. The peak deconvolution matches the experimental data with a sharp low stiffness peak at 149 MPa and a broader peak at 334 MPa.

According to the qualitative map analysis, described in Fig. 3, the sharp low stiffness peak is associated with the ionomer, while the broader high stiffness peak is associated with Pt catalyst particles. Sharp ionomer and broad catalyst peaks were identified in each analyzed histogram. Averaging the peak positions of the same domain types (pristine, operated, operated—within CF imprint) yields the results displayed in Fig. 4b. The shown statistical

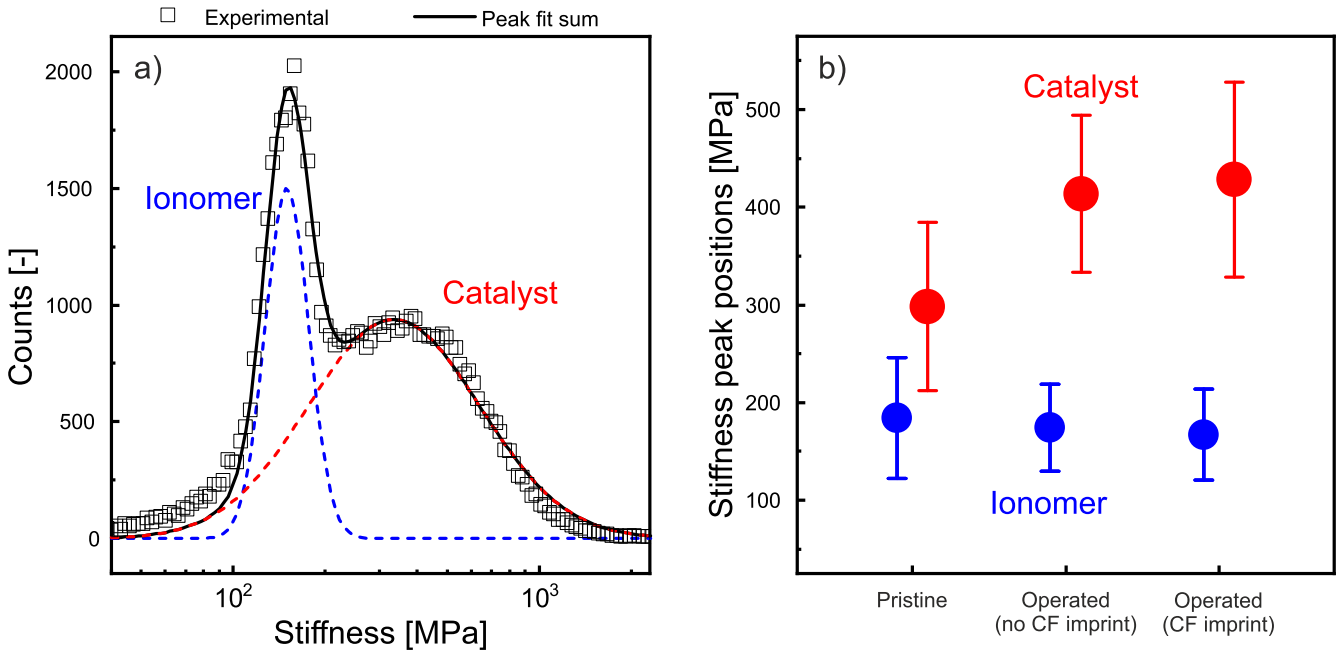

Figure 4. (a) The stiffness histogram was derived from the 5 µm · 5 µm stiffness map, shown in Fig. 3c. The peak deconvolution ($R^2 = 0.99$) reveals a sharp low stiffness peak and a broader high stiffness peak—the former is associated with the ionomer and the latter with the Pt catalyst. (b) The histograms acquired from stiffness maps recorded at multiple positions (see Fig. S1) were deconvoluted and the averaged ionomer and catalyst peak positions are presented for the pristine and operated sample. Operated positions were split up depending on CF imprints. No significant change of the ionomer stiffness is indicated, while the catalyst stiffness increases.

deviations indicate the standard deviation of the peak positions. While the ionomer on pristine sample positions exhibits an average stiffness of 184 ±62 MPa, the ionomer stiffness on the operated cathode surface was found to be 175 ±45 MPa, and 167 ±47 MPa for positions outside and within CF imprints, respectively. The catalyst peaks are shifted toward higher stiffnesses for the operated cathode. Pristine cathode's catalyst peaks are located at 298 ±87 MPa, while operated cathode's catalyst peaks are located at 414 ±81 MPa and 428 ±100 MPa for positions outside and within CF imprints, respectively.

As the measured stiffness is in the range of typical PFSA ionomers,[37,38] and not of Pt,[39] the ionomer or underlying pores determine the cathode's nanomechanical response. No clear change in the ionomer stiffness is observed upon operation. While the average ionomer stiffness is lowered slightly, e.g. by 17 MPa at position within CF imprints at the operated cathode, this decrease is within the statistical deviations of pristine positions. The statistical deviations of the ionomer stiffness are bolstered by the occurence of locally different ionomer domains, even within 5 µm · 5 µm areas. Figure S3 shows areas where the stiffness of neighboring ionomer domains locally vary around 100 MPa. While it is reported in literature, that restructuring of the ionomer upon operation takes place,[40] there is no information available, to what extent such a restructuring of the ionomer reflects onto the local surface stiffness, and if that might be resolved by nanomechanical AFM. Furthermore, crystallite regions on ionomers are reported,[41] that have different nanomechanical properties. Therefore, based on the current results, deviations in the ionomer stiffness might be associated with either, locally different structural or chemical properties of the PFSA or varying thicknesses of the ionomer plateaus. Thin film ionomer at the catalyst interface was reported to have a different structure compared to bulk ionomer.[42–44] As the surface ionomer stiffness remains constant with comparable statistical deviations upon operation, it seems that the causes for the varying local ionomer stiffnesses do not escalate or diminish upon operation. While the ionomer plateaus show no signs of aging, a stiffening is observed at the catalyst particles. No difference in catalyst stiffness was observed between positions within CF imprints, compared to those outside. Local PTL related phenomena, which are reported in literature, such as increased current densities,[29] and varied porosity at PTL imprints,[28] might be not significant for the local surface cathode aging. In a fuel cell study it was reported that thin ionomer films, that surround the catalyst particles thin upon operation.[45] Thus, a stiffness increase of the catalyst particles might be observed due to a thinning of low-stiffness ionomer films, which surround the catalyst particles or due to catalyst rearrangements. Likely, the stiffening is not observed due to compression or densification of the material, as there is no difference observed between the compressed regions within the fiber imprints and those outside.

The slight increase in catalyst stiffness on the surface is in agreement with the sligthly increased overall mean reduced modulus of the cathode bulk, shown by the nanoindentations (Fig. 2). The previously observed heterogenization of the cathode bulk is not observed on the surface. Therefore, the cause for heterogenization might be rather within the bulk or the membrane-cathode interface.

Nanoelectrics.—Beside the stiffness maps, that were statistically evaluated, contact current maps give insights into the ionomer and catalyst distribution on the surface. 20 µm · 20 µm contact current maps were acquired randomly, and thus provide information about the surface distribution of electrically conductive catalyst and electrically insulating ionomer. Figure 5a and 5b display the topography map and simultaneously acquired contact current map of a pristine cathode, respectively. A binary contact current map, shown in Fig. 5c, displays only the electrically conductive surface area. The area is considered as electrically conductive, if a contact current above background noise (10 pA) was measured. Additionally, the conductive surface area fraction presents the overall fraction of pixels that match this criteria. A conductive surface area fraction of 73.0 % was found on the pristine position. For an operated cathode position comprising a CF imprint, Figs. 5d–5f show a topography, contact current, and binary contact current map, respectively. The binary contact current map reveals a conductive surface area fraction of 73.7 %. The averaged conductive surface area fractions of multiple positions are displayed in Fig. 5g. Pristine cathode areas exhibit a conductive surface area fraction of 71.0 ±9.2 %, while these of operated areas are 65.0 ±15.8 % and 73.4

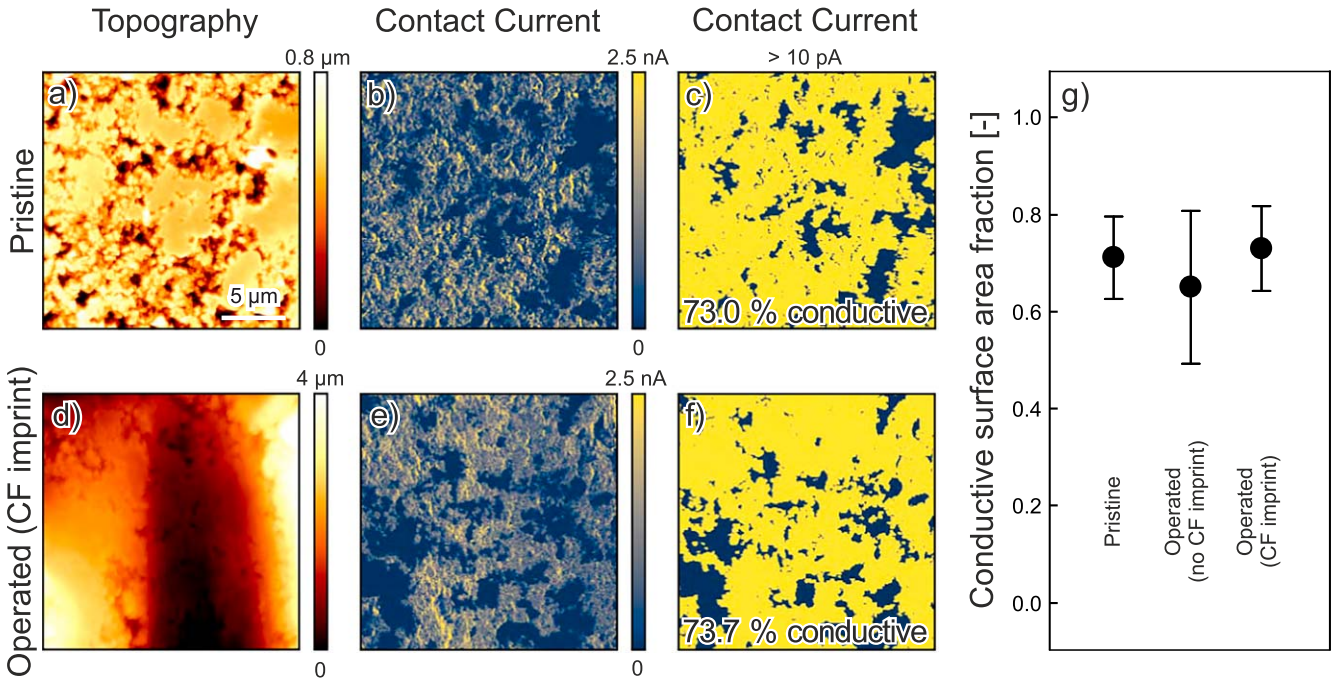

Figure 5. (a) The 20 µm · 20 µm topography map of a pristine cathode is displayed. (b) The respective contact current map exhibits that the surface is mostly electrically conductive, while there are a few areas at which no current was measured. (c) A threshold of 10 pA is applied to the contact current map to yield a binary image of the conductive pixels. The conductive surface area fraction is 73.0 %. (d) The 20 µm · 20 µm topography map of an operated cathode with a CF fiber imprint is displayed. (e) The corresponding contact current map reveals that similar currents are measured across the analyzed area—within the imprint and next to it. (f) The binary image of the contact current map yields a conductive surface area fraction of 73.7 %. (g) The conductive surface area fractions derived from the binary images, as shown in (c) and (f), are averaged across the multiple analyzed 20 µm · 20 µm positions of the same type (pristine, operated, operated with CF imprint). The results show a rather constant conductive surface area fraction with operation.

±9.3 % for positions outside CF imprint and within CF imprints. According to the results, no clear change in conductive surface area fraction upon operation is observed, as statistical deviations show a significant overlap. This is in agreement with literature, where a constant conductive surface area fraction on the cathode was observed.[25]

As described in Fig. 3, electrically non-conductive areas are associated with ionomer areas. Thus, the high conductive surface area indicates that electrically conductive catalyst particles are well distributed across the cathode surface, with only smaller fractions of insulating ionomer areas. Upon operation, the ionomer coverage remains constant. The constant ionomer surface coverage accompanied by the constant stiffness of the ionomer plateaus indicate the stable nature of such areas at the cathode surface. In general, the cathode surface appears long-term stable and suitable for industrial application. The ionomer content in electrodes influences the macroscopic performance.[46,47] While low ionomer contents results in higher proton conduction resistances, high ionomer contents might lead to a filling of the electrode void volume, thus leading to higher gas mass transport and increased electronic contact resistance.[46] Ultimately, the high fraction of conductive surface area, observed on the cathode (see Fig. 5), indicates a potentially good electrical contact to the CF PTL. The electrical contact is only hindered at certain µ*m*-sized ionomer plateaus.

Conclusions

Optimize PEMEC MEAs for economically viable electrochemical hydrogen production is one of the highest priorities for the energy transition, which necessitates the analysis of long-term operated MEAs. By conducting nanoelectrical and nanomechanical analysis on pristine and operated web-woven fiber reinforced MEAs, valuable insights concerning durability have been uncovered. This work analyzes the cathode and extends the results, that have already been published for the anode. While on the anode the surface ionomer fraction was diminished and significant aging especially at PTL contact areas was observed upon operation,[26] the cathode underwent only a slight change in nanomechanics and nanoelectrics.

Nanoindentation reveals a slight increase of the cathode's mean reduced modulus and hardness upon operation, while a heterogenization is observed. To unravel the surface contribution to the observed nanomechanical changes, nanoelectrical and nanomechanical PF-TUNA was performed. Thus, the surface distribution on pristine and operated samples of the two distinct species—low stiffness and electrically non-conductive ionomer pleateaus and high stiffness electrically conductive catalyst particles—were revealed. On operated samples, additional CF imprints originating from the PTL contact during operation are observed. Statistical evaluation of multiple PF-TUNA maps uncovers the main findings: First, the fraction of ionomer plateaus on the surface as well as their stiffness remained constant upon operation. Thus, no signs of degradation at such ionomer plateaus are observed. While the ionomer plateaus exhibit constant properties upon operation, local ionomer domains of varying stiffness values are observed that either indicate ionomer domains of varying thicknesses or locally varying structural or chemical properties. Second, the stiffness of catalyst particles increased equally upon operation at both domains—within CF imprints and outside of CF imprints. Thus, the locally different environment around CF PTL imprints, e.g. by increased current densities or more compressed pores, do not affect the assessed surface aging noticeably. Third, the stiffening of the surface catalyst particles, shown by PF-TUNA, contribute to the slightly increased reduced modulus of the cathode bulk. However, the observed heterogenizations of the cathode bulk are rather associated to changes in the cathode bulk or around the cathode-membrane interface.

For future research, a deeper insight into the cathode bulk and the cathode-membrane interface are required. As hydrogen ions enter the cathode layer at the membrane interface, the aging might be enhanced around that interface, while the cathode-PTL interface

might remain more stable. Micro- and nanoscale analysis of the catalyst and ionomer distribution in the bulk could provide more complete insights into local electric and ionic conductivity limitations. Moreover, assessing the influence of layer thickness and different PFSA properties on the observed surface stiffness will help to interpret the occurrence of locally different ionomer domains.

Experimental

MEA The MEA sample was taken out from a durability test run. The MEA was provided by Siemens Energy consisting of a reinforced PFSA) membrane with a Pt-based cathode and an Ir-based anode. Operation hours were cumulated over more than 5000 h. A CF PTL was used on the cathode. Pristine and operated MEAs were cut at equivalent positions for analysis. The cut samples were positioned equally distanced from water inflow and outflow (see Fig. S1). Furthermore, two pieces, equally distanced from the MEA center were analyzed to enhance the statistics. Operated samples were dried before characterization.

SEM An AMBER X (TESCAN, Czech Republic) SEM was utilized at high vacuum mode and room temperature. 0.5 cm · 0.5 cm samples fixed with conductive carbon tape were imaged with a working distance of 6 mm, utilizing a secondary electron detector (Everhart-Thornley, E-T). A beam acceleration of 2 keV, a sample current of 300 pA, and a dwell time for each pixel of 3.2 µs were utilized.

Nanoindentation The nanoindentations were performed with a Hysitron TI 980 (Bruker, USA) with a Berkovich tip at ambient conditions. 1 cm · 1 cm samples were cut and glued with cyanoacrylate glue onto a stainless steel substrate ensuring there was no air between MEA and substrate. 360 µm · 360 µm maps were acquired by performing 18 · 18 indents with 20 µm spacing between each indent, preventing an overlap of indented areas. Indents were performed force controlled with constant load and unload rates of 160 µN s^{-1} for 5 s. The resulting maximum load of 800 µN was hold constant for 2 s in between unload and load phases. Reduced modulus and hardness were determined by TriboScan Analysis software (Bruker, USA) with the Oliver-Pharr Model.[48] The hardness is a measure of the cathode's resistance to localized plastic deformation, while the reduced modulus is a measure of the cathode's elastic response with contributions from the indenter.

PF-TUNA AFM measurements were performed with a Dimension Icon (Bruker, USA) in the current sensing and force-distance curve based PeakForce tunneling atomic force microscopy mode (PF-TUNA, Bruker, USA) at ambient conditions. The anode side was mounted with double sided tape onto a steel disc. Additional conductive carbon tape, mounted on top of one cathode side of the 1 cm^2 samples, ensured good electrical contact. The applied bias voltage was 20 mV and the current sensitivity was 1 nA V^{-1}. PPP-NCSTPt cantilevers (Nanosensors, Switzerland) with determined spring constants between 16 N m^{-1} to 20 N m^{-1} and an electrically conductive $PtIr_5$ coating on the silicon tip have been individually calibrated performing five ramps onto a sapphire sample (Bruker, USA). The deflection sensitivity and spring constant were calculated utilizing the Nanoscope software (9.4r2, Bruker, USA) from the retraction part of each ramp and averaged. 5 µm · 5 µm maps for statistical analysis were measured with a constant maximum normal load of 40 nN and a slow scan rate of 0.3 Hz. The scans consists of 256 · 256 Pixels. The recorded contact current is the current averaged over the tip-sample contact duration during each tapping cycle. The 0.5 µm · 0.5 µm high resolution scan was acquired with a scan rate of 0.5 Hz, while the residual parameters were the same as for the 5 µm · 5 µm maps. The stiffness provides information about the cathode's resistance to elastic deformation and refers to the reduced modulus which was calculated from the force-distance curves with the Derjaguin, Muller, Toporov (DMT) model.[49] To recalculate the tip radius, which is needed for DMT model calculations,[50] the polystyrene of the PS-LDPE-12M sample (Bruker, USA) with a nominal stiffness of 2 GPa was utilized as reference.

The stiffness histograms were derived from analysis of the 5 µm · 5 µm stiffness maps and display the pixel counts and their respective stiffness. The classification was performed with 200 bins, with logarithmically equal size, between 10 MPa to 5000 MPa. The peaks were fitted with log-normal distributions shifted on the x-axis. As a basis for the AFM data processing, the pySPM package (v0.2.20) for python was utilized.[51] All shown topograhy maps were first order slope corrected.

Acknowledgments

The authors gratefully acknowledge the financial support by the German Federal Ministry of Education and Research (BMBF) within the H2Giga project DERIEL (grant number 03HY122C). The authors declare no conflict of interest. Data for this article, including the AFM and nanoindentation data, are available at Jülich DATA at https://doi.org/10.26165/JUELICH-DATA/XF24KT.

ORCID

Julian Borowec https://orcid.org/0000-0003-3290-500X
Jean-Pierre Poc https://orcid.org/0009-0005-8675-5547
Shibabrata Basak https://orcid.org/0000-0002-4331-4742
Günter Schmid https://orcid.org/0000-0001-7836-5171
Eva Jodat https://orcid.org/0009-0004-8214-2981
André Karl https://orcid.org/0000-0003-2289-5987
Rüdiger-A. Eichel https://orcid.org/0000-0002-0013-6325
Florian Hausen https://orcid.org/0000-0001-5712-6761

References

1. Q. Feng, X.-Z. Yuan, G. Liu, B. Wei, Z. Zhang, H. Li, and H. Wang, *Journal of Power Sources*, **366**, 33 (2017).
2. W. Li, Y. Bu, X. Ge, F. Li, G.-F. Han, and J.-B. Baek, *ChemSusChem*, e202400295 (2024).
3. C. Wang et al., *ChemSusChem*, **12**, 1576 (2019).
4. J. Li, W. Tian, Q. Li, and S. Zhao, *ChemSusChem*, e202400239 (2024).
5. C. Liu et al., *J. Electrochem. Soc.*, **170**, 034508 (2023).
6. C. Liu et al., *Adv. Energy Mater.*, **11**, 2002926 (2021).
7. S. Siracusano, V. Baglio, N. van Dijk, L. Merlo, and A. S. Aricò, *Applied Energy*, **192**, 477 (2017).
8. C. Rakousky, U. Reimer, K. Wippermann, M. Carmo, W. Lueke, and D. Stolten, *Journal of Power Sources*, **326**, 120 (2016).
9. F. Andolfatto, R. Durand, A. Michas, P. Millet, and P. Stevens, *International Journal of Hydrogen Energy*, **19**, 421 (1994).
10. Y. Kobayashi, K. Kosaka, T. Yamamoto, Y. Tachikawa, K. Ito, and K. Sasaki, *International Journal of Hydrogen Energy*, **39**, 16263 (2014).
11. F. Lapicque, M. Belhadj, C. Bonnet, J. Pauchet, and Y. Thomas, *Journal of Power Sources*, **336**, 40 (2016).
12. M. Chandesris, V. Médeau, N. Guillet, S. Chelghoum, D. Thoby, and F. Fouda-Onana, *International Journal of Hydrogen Energy*, **40**, 1353 (2015).
13. H. Liu, F. D. Coms, J. Zhang, H. A. Gasteiger, and A. B. LaConti, *Polymer Electrolyte Fuel Cell Durability* (Springer, New York)71 (2009).
14. S. Grigoriev, P. Millet, S. Volobuev, and V. Fateev, *International Journal of Hydrogen Energy*, **34**, 4968 (2009).
15. A. Kusoglu and A. Z. Weber, *The Journal of Physical Chemistry Letters*, **6**, 4547 (2015).
16. A. Kusoglu, M. Calabrese, and A. Z. Weber, *ECS Electrochem. Lett.*, **3**, F33 (2014).
17. Y.-H. Lai, C. Gittleman, F. D. Coms, S. Kumaraguru, Z. Green, B. Zackin, and C. Mittelsteadt, *J. Electrochem. Soc.*, **172**, 024504 (2025).
18. H. Yu, L. Bonville, J. Jankovic, and R. Maric, *Applied Catalysis B: Environmental*, **260**, 118194 (2020).
19. A. Kusoglu, S. Savagatrup, K. T. Clark, and A. Z. Weber, *Macromolecules*, **45**, 7467 (2012).
20. R. Kuwertz, C. Kirstein, T. Turek, and U. Kunz, *Journal of Membrane Science*, **500**, 225 (2016).
21. M. G. De Angelis, S. Lodge, M. G. Baschetti, G. C. Sarti, F. Doghieri, A. Sanguineti, and P. Fossati, *Desalination*, **193**, 398 (2006).
22. T. Morawietz, *Ph.D. thesis, University of Stuttgart* (2022).
23. S. Siracusano, N. van Dijk, R. Backhouse, L. Merlo, V. Baglio, and A. S. Aricò, *Renewable Energy*, **123**, 52 (2018).
24. S. A. Grigoriev, K. Dzhus, D. G. Bessarabov, and P. Millet, *International Journal of Hydrogen Energy*, **39**, 20440 (2014).
25. P. Lettenmeier et al., *Electrochimica Acta*, **210**, 502 (2016).
26. J. Borowec, L. Rein, N. Gorin, S. Basak, L. Dobrenizki, G. Schmid, E. Jodat, A. Karl, R.-A. Eichel, and F. Hausen, *Journal of Materials Chemistry A*, **13**, 6347 (2025).

27. C. Heume et al., *Research Square* (2024), [Preprint version 1] (2024), https://doi.org/10.21203/rs.3.rs-5337119/v1.
28. K. J. Ferner, J. Park, Z. Kang, S. A. Mauger, M. Ulsh, G. Bender, and S. Litster, *International Journal of Hydrogen Energy*, **59**, 176 (2024).
29. Y. Pan, H. Liu, J. Liu, L. Wen, K. Lao, S. Li, X. Fang, H. Wang, H. B. Tao, and N. Zheng, *Catalysis Science & Technology*, **14**, 6 (2024).
30. I. Kundler et al., (2023), ,Accessed February 2025, https://www.wasserstoff-leitprojekte.de/lw_resource/datapool/systemfiles/elements/files/05C4AF0039AB2C08E0637E695E863F24/current/document/H2Giga_Projektbrosch%C3%BCre.pdf.
31. M. R. VanLandingham, J. S. Villarrubia, W. F. Guthrie, and G. F. Meyers, *In Macromolecular Symposia*, **167**"Wiley Online Library."15 (2001).
32. J. Borowec, V. Selmert, A. Kretzschmar, K. Fries, R. Schierholz, H. Kungl, R.-A. Eichel, H. Tempel, and F. Hausen, *Adv. Mater.*, 2300936 (2023).
33. K. Poornesh, C. Cho, G. Lee, and Y. Tak, *Journal of Power Sources*, **195**, 2709 (2010).
34. K. Poornesh and C. Cho, *International Journal of Hydrogen Energy*, **36**, 3623 (2011).
35. Y. Shen, *Ph.D. Thesis, University of Waterloo* (2017).
36. H. Becker, J. Murawski, D. V. Shinde, I. E. Stephens, G. Hinds, and G. Smith, *Sustainable Energy & Fuels*, **7**, 7 (2023).
37. A. Kusoglu, Y. Tang, M. Lugo, A. M. Karlsson, M. H. Santare, S. Cleghorn, and W. B. Johnson, *Journal of Power Sources*, **195**, 483 (2010).
38. M. B. Satterfield and J. B. Benziger, *Journal of Polymer Science Part B: Polymer Physics*, **47**, 11 (2009).
39. R. Farraro and R. B. Mclellan, *Metallurgical Transactions A*, **8**, 1563 (1977).
40. R. Hiesgen, T. Morawietz, M. Handl, M. Corasaniti, and K. A. Friedrich, *J. Electrochem. Soc.*, **161**, F1214 (2014).
41. M. Bass, A. Berman, A. Singh, O. Konovalov, and V. Freger, *The Journal of Physical Chemistry. B*, **114**, 3784 (2010).
42. P. Vanya, J. Sharman, and J. A. Elliott, *The Journal of Chemical Physics*, **147** (2017).
43. P. Ferreira et al., *J. Electrochem. Soc.*, **152**, A2256 (2005).
44. R. Jinnouchi, K. Kudo, K. Kodama, N. Kitano, T. Suzuki, S. Minami, K. Shinozaki, N. Hasegawa, and A. Shinohara, *Nat. Commun.*, **12**, 4956 (2021).
45. T. Morawietz, M. Handl, C. Oldani, P. Gazdzicki, J. Hunger, F. Wilhelm, J. Blake, K. A. Friedrich, and R. Hiesgen, *J. Electrochem. Soc.*, **165**, F3139 (2018).
46. M. Bernt and H. A. Gasteiger, *J. Electrochem. Soc.*, **163**, F3179 (2016).
47. W. Xu and K. Scott, *International Journal of Hydrogen Energy*, **35**, 12029 (2010).
48. W. C. Oliver and G. M. Pharr, *J. Mater. Res.*, **7**, 1564 (1992).
49. B. V. Derjaguin, V. M. Muller, and Y. P. Toporov, *J. Colloid Interface Sci.*, **53**, 314 (1975).
50. T. J. Young, M. A. Monclus, T. L. Burnett, W. R. Broughton, S. L. Ogin, and P. A. Smith, *Meas. Sci. Technol.*, **22**, 125703 (2011).
51. O. Scholder, (2019), scholi/pyspm v0.2.20, https://doi.org/10.5281/zenodo.998575.